

# Waste-derived char-supported Ni catalyst for syngas methanation: Ni recovery, performance evolution and its implications for assessing char support

Zhenfei Mei <sup>a,b</sup>, Hongquan Zhou <sup>a</sup>, Shaoheng Ge <sup>a,b</sup>, Yuheng Feng <sup>a,b</sup>, Dezhen Chen <sup>a,b,\*</sup>

<sup>a</sup> Thermal and Environmental Engineering Institute, School of Mechanical Engineering, Tongji University, 1239 Siping Road, Shanghai 200092, China

<sup>b</sup> Shanghai Engineering Research Center of Multi-source Solid Wastes Co-processing and Energy Utilization, Shanghai 201804, China



## ARTICLE INFO

### Keywords:

Municipal solid waste-derived char  
Syngas methanation  
Catalyst  
Ni recovery  
Alkali-carbon index

## ABSTRACT

Syngas methanation was studied using the regenerated Ni-based catalyst supported on municipal solid waste-derived char (Ni/MSWC). Catalysts were prepared by recovering Ni from the spent Ni/MSWC via an acid-assisted process and their performance evolution was analyzed by experiments and density functional theory (DFT) calculations. The regenerated catalysts showed similar methanation activity to the original with a CH<sub>4</sub> yield of ~90 % but repeated acid-assisted recovery carried the risk of deactivating the catalyst, due to the enrichment of acid-soluble minerals from the char carrier. The ash composition of char carriers quantified with an alkali-carbon index of ~20 could be an indicator for assessing the char carriers. DFT insights proved defect-induced Ni particle adsorption on MSWC and the improved electronic structure of Ni particles induced by the active acid-soluble minerals. This research highlights the potential of utilizing MSWC and recovered Ni for sustainable methanation catalysts and provides implications for choosing qualified waste-derived char carriers.

## 1. Introduction

Waste-to-energy technology, especially the recovery of value-added energy products from municipal solid waste (MSW), has emerged as a crucial concern in the field of renewable energy development. Compared to conventional incineration technology, the MSW pyrolysis process is more effective in preventing the formation of dioxins and reducing NO<sub>x</sub> emissions [1]. Furthermore, as an energy converter, pyrolysis devices recover char, oil (or liquid product), and syngas from MSW; in addition, pyrolysis technology exhibits flexibility in scale, making it suitable for managing MSW in small-scale and decentralized conditions. To refine the pyrolysis products to meet market demands, a conversion route of "MSW - syngas - methane" has been proposed [2], which produced high-quality CH<sub>4</sub> or CH<sub>4</sub>-rich fuel gas from MSW cost-effectively by using MSW-derived char-supported Ni catalysts (Ni/MSWC) for methanation step. MSW pyrolysis char (MSWC) is cheap and easily available as a carbonaceous carrier. The in-situ conversion of MSW-derived syngas into methane offers a promising solution to distributed waste management, as methane can be easily integrated into the existing natural gas pipeline network, as well as utilized in local

factories. However, a reliable Ni/MSWC is the key to this conversion route. The heterogeneous characteristics of the MSW lead to the unstable composition of MSWC, thus its reliability to be used as the catalyst carrier is doubtful.

The activity of Ni/MSWC is related to the following factors [3–5]: porous structure of the char carrier, oxygen-containing groups present on the char surface, and inorganic ash in the char. The ash composition of the char carrier is closely related to the methanation activity of the char-based catalyst [5], especially the alkali and alkaline earth metals (AAEMs) and Fe contents [6,7]. In previous research [5], the role of inorganics in the waste-derived char on the methanation reaction was identified by adopting water and acid washing to remove part of the ash from the char, but it did not achieve a regular control of the content of AAEMs, particularly failing to increase their content in the char. Furthermore, AAEMs in MSWC can change the adsorption ability of the catalyst on CO<sub>2</sub>, and under conditions where both CO and CO<sub>2</sub> are present, the hydrogenation mechanism of CO and CO<sub>2</sub> over a Ni/MSWC with rich AAEMs are unclear. Moreover, the promotional effect of AAEMs on Ni has not been explored essentially from a molecular perspective, so it cannot guide the design of the catalyst.

\* Corresponding author at: Thermal and Environmental Engineering Institute, School of Mechanical Engineering, Tongji University, 1239 Siping Road, Shanghai 200092, China.

E-mail address: [chendezhen@tongji.edu.cn](mailto:chendezhen@tongji.edu.cn) (D. Chen).

In addition to its availability, another important benefit of Ni/MSWC catalyst is its recyclability. Upon deactivation, Ni can be easily recovered from the spent catalyst by burning the spent one and subsequently recovering Ni from the ash. Strong acids or bases are often adopted to leach the active metals from the spent catalyst [8], followed by additional methods such as evaporation & crystallization to obtain pure metal compounds [9]. Compared with the traditional refractory carriers such as  $\text{Al}_2\text{O}_3$  and  $\text{SiO}_2$ , char-supported catalysts are less prone to forming  $\text{NiAl}_2\text{O}_4$  and  $\text{NiSiO}_3$  which have higher resistance towards acid extraction [10], thus ensuring a high Ni recovery rate. Recovering Ni from the spent catalysts by strong acid such as  $\text{HNO}_3$  extraction will inevitably dissolve the acid-soluble minerals such as salts of AAEMs and other transition metals (e.g., Fe), attributed to the complex ash composition present in the MSWC carrier [5]. If both the recovered Ni and AAEMs in the acid-washing solution are used for the preparation of the new catalysts, for the same MSWC, the resultant catalysts will have a regular increase in their ash and AAEMs contents, thus, the influence of the higher content of AAEMs on the catalyst performance can be evaluated. Deactivation reasons of the catalysts may include [11]: carbon deposition, poisoning, and structural damage. Poisoning by HCl and  $\text{H}_2\text{S}$  often leads to an irreversible increase in Ni particle size [12,13]. As chlorine is widely available in MSW [14], HCl is released in much higher quantities in crude syngas from MSW compared to  $\text{H}_2\text{S}$  [15]. During the pyrolysis process, HCl concentration can reach up to 70 mg/Nm<sup>3</sup> [16]. Hence, in this study, HCl is chosen as a representative contaminant to intentionally deactivate the Ni/MSWC catalyst, allowing Ni recovery to be performed based on a deactivated catalyst. In addition, after the acid treatment of the spent catalyst, the way of reusing the acid-washed solution for subsequent catalyst preparation needs further clarification: to use the whole solution or to obtain the Ni-containing salts by evaporating the solution.

In this research, acid-assisted Ni recovery is adopted for recovering Ni from the spent Ni/MSWC catalysts poisoned by HCl. The influence of acid-assisted recovery number will be checked, which leads to the accumulation of acid-soluble minerals in the extraction solution, ultimately changing the ash content of the char carrier, on the catalytic performance, aiming to understand the composition of MSWC as a reliable catalyst carrier. To define an appropriate acid-assisted recovery and reuse pathway for spent catalysts, two pathways using the acid-washed extract for char-based catalyst preparation will be compared: one is direct impregnation with the acidic extraction solution, and another is to evaporate the solution to recover solid-phase Ni salts, followed by dissolving the salts in ethanol for impregnation. Density functional theory (DFT) and in situ DRIFTS will be performed to investigate the CO& $\text{CO}_2$  methanation pathway over Ni/MSWC, as well as to understand the potential interactions between the carbonaceous carrier and surface minerals with the active metal Ni. The primary objective of this research is to establish a theoretical framework for the application of waste-derived char catalysts.

## 2. Materials and methods

### 2.1. Materials

The municipal solid waste (MSW) sample was obtained from an incineration plant in Shanghai. Following solar drying in a greenhouse and the subsequent removal of inorganic components such as glass and stones, the MSW sample was further shredded into pieces smaller than 10 mm. The analysis results on MSW components and the characteristics of the MSWC can be found in Table 1. The high ash content up to 69.12 wt% in the MSWC was attributed to the high ash content of the residue component in MSW. The ash was primarily composed of  $\text{SiO}_2$  and  $\text{CaCO}_3$ , as shown in Fig. S1.

**Table 1**  
Properties of MSW and MSWC.

Material	Property	Component	value
MSW	Physical composition (wt%, ad <sup>a</sup> )	Kitchen wastes	25
		Paper	10
		Cloth	25
		Plastics	20
		Residue	20
MSWC	Proximate analysis (wt%, db <sup>b</sup> )	Ash	69.12
		Volatile	7.01
		Fixed carbon	23.87
	Ultimate analysis (wt%, db)	C	25.84
		H	0.94
		N	0.41
		O <sup>c</sup>	3.68
		S	0.01

<sup>a</sup> ad: air-dry basis.

<sup>b</sup> db: dry basis.

<sup>c</sup> O: by difference

### 2.2. Catalyst preparation

To obtain MSWC for preparing the catalyst, MSW samples underwent pyrolysis in a tube pyrolysis reactor at a temperature of 600 °C with a heating rate of 10 °C·min<sup>-1</sup>. The obtained MSWC was ground into powder with a size smaller than 1 mm, then it was utilized as the catalyst carrier. The original fresh catalyst was prepared by the impregnation method, using  $\text{Ni}(\text{NO}_3)_2 \cdot 6 \text{H}_2\text{O}$  as the Ni precursor. The designed loading amount of Ni in the catalyst was 20 wt%, while the actually achieved loading amount was 19.7 wt%. The Ni recovery from the spent catalyst is represented in Fig. 1, which was conducted using  $\text{HNO}_3$  extraction, and the parameters of  $\text{HNO}_3$  concentration, leaching time, and temperature were referenced to those reported by Sheik *et al.* [17], to optimize the leaching efficiency of Ni. The Ni recovery rate from the spent catalysts was verified to be above 99.5 % by using ICP analysis. When reusing the recovered Ni to prepare the new catalyst, whether the residual  $\text{HNO}_3$  in the Ni extraction solution should be evaporated or not was evaluated by comparing two methods: the first method involved impregnating the fresh MSWC with the original extraction solution containing Ni salt and residual  $\text{HNO}_3$  (Fig. 1(a)), and the second one was evaporating the extraction solution to recover the solid Ni salts (Fig. 1(b)); then the Ni salts were dissolved into an ethanol solution to impregnate the fresh MSWC. The detailed impregnation, calcination, and reduction conditions are also shown in Fig. 1. In Fig. 1(a), the residual  $\text{HNO}_3$  in the extraction solution could improve the surface characteristics of the char, enhancing its hydrophilicity [18]. This facilitated the accessibility of the char surface to aqueous metal precursors. In Fig. 1(b), after the extraction solution was evaporated, low-polarity ethanol was used to dissolve the Ni salts instead of water, followed by impregnation onto MSWC. Its low-polarity also favored the accessibility of the char surface to metal precursors [19], which improved the performance of the prepared catalyst compared with using an aqueous solution of Ni salts (Fig. S2).

“RX” was used to indicate the catalyst prepared after the  $X_{th}$  of the Ni recovery and reuse cycle, according to the method described in Fig. 1. For example, R0 indicates the original fresh Ni/MSWC catalyst, while R1, R2, and R3 represent the catalysts prepared for the first, second, and third Ni recovery and reuse cycles, respectively.

### 2.3. Catalyst deactivation with HCl and performance evaluation

The activity test was conducted using a fixed-bed reactor equipped with a porous support at the center position, as depicted in Fig. 2. For each experimental run, a fixed-bed reactor was created by placing 5 g of catalyst on the porous support, and the syngas with arranged composition passed through the catalyst layer. A 10-hour continuous methanation process was adopted to evaluate the short-term performance of catalysts. The reactor was running at atmospheric pressure under the

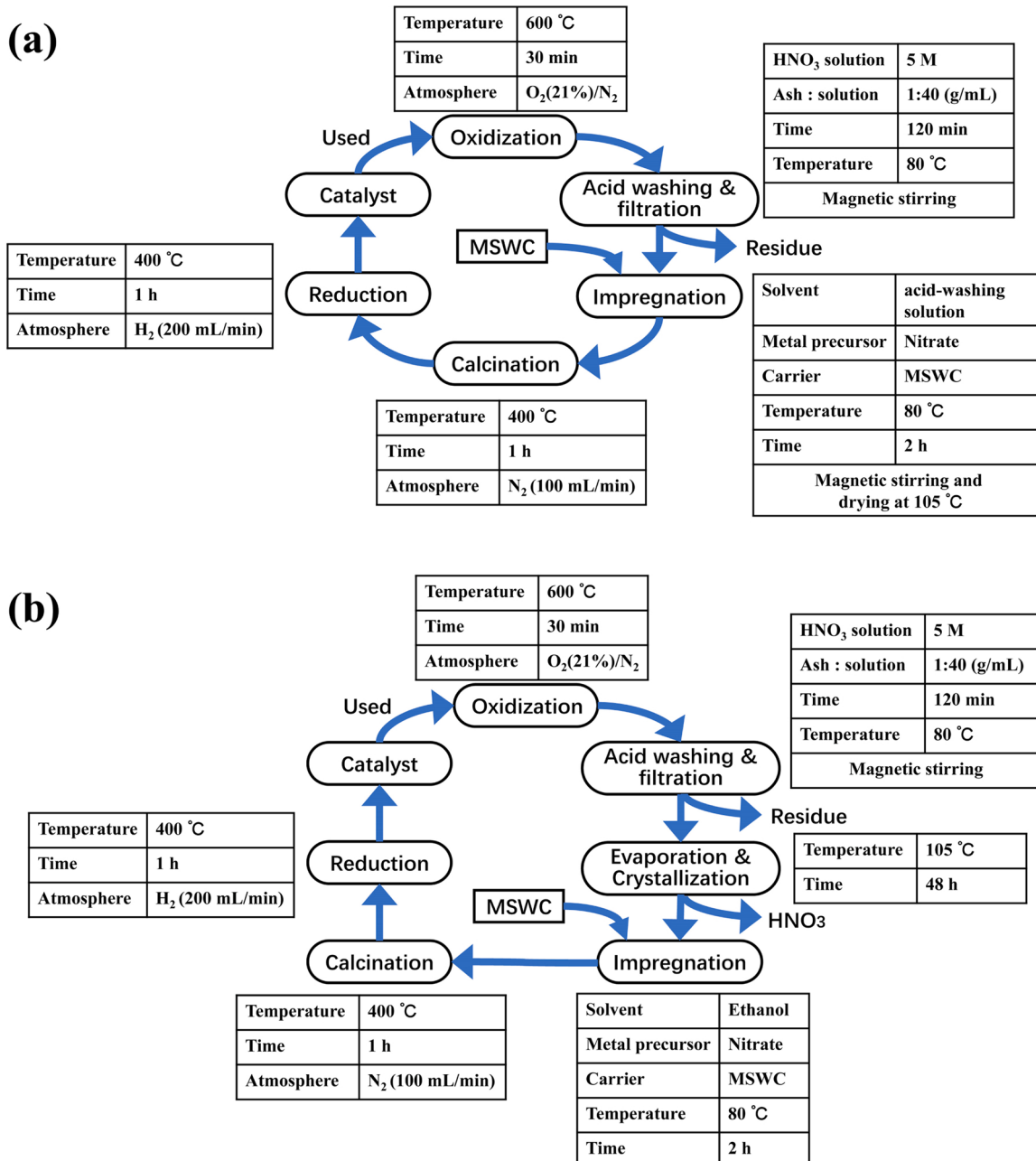


**Fig. 1.** Ni recovery and reuse methods: (a) direct impregnation with the acidic extraction solution; (b) Evaporating acidic extraction solution to obtain Ni-containing salts for impregnation.

temperature of 400 °C.

The arranged syngas consisted of H<sub>2</sub> (62.7 vol%), CO (9.4 vol%), CO<sub>2</sub> (6.3 vol%), H<sub>2</sub>O (0/6 vol%), HCl (0/100/200 ppmv), and N<sub>2</sub> (for balance), with the flow rates of H<sub>2</sub>, CO, and CO<sub>2</sub> being 240, 36, and 24 mL/min respectively, and the gas hourly space velocity was about 3200 h<sup>-1</sup>. Here HCl was adopted to deactivate the Ni/MSWC catalyst. A cold trap was used to remove the water vapor in the gas product. Subsequently, the gas product was collected using a gas collection bag and analyzed offline for its gas composition with the help of a gas chromatograph (7820 A, Agilent, USA). The conversion rate (X), selectivity (S), and yield (Y) of the reaction were calculated using Eqs. (1) to (5), where the subscripts "in" and "out" correspond to the inflow and outflow gases, and CO<sub>in</sub> and CO<sub>out</sub> are the mole numbers of CO at the inlet and outlet of the reactor, respectively; the same for other gas components.

$$X_{CO} = \frac{CO_{in} - CO_{out}}{CO_{in}} \times 100\% \quad (1)$$

$$X_{CO_2} = \frac{CO_{2in} - CO_{2out}}{CO_{2in}} \times 100\% \quad (2)$$

$$X_{CO_x} = \frac{CO_{in} + CO_{2in} - CO_{out} - CO_{2out}}{CO_{in} + CO_{2in}} \times 100\% \quad (3)$$

$$S_{CH_4} = \frac{CH_4_{out}}{CO_{in} + CO_{2in} - CO_{out} - CO_{2out}} \times 100\% \quad (4)$$

$$Y_{CH_4} = \frac{CH_4_{out}}{CO_{in} + CO_{2in}} \times 100\% \quad (5)$$

To evaluate the impact of changes in char carrier's composition on

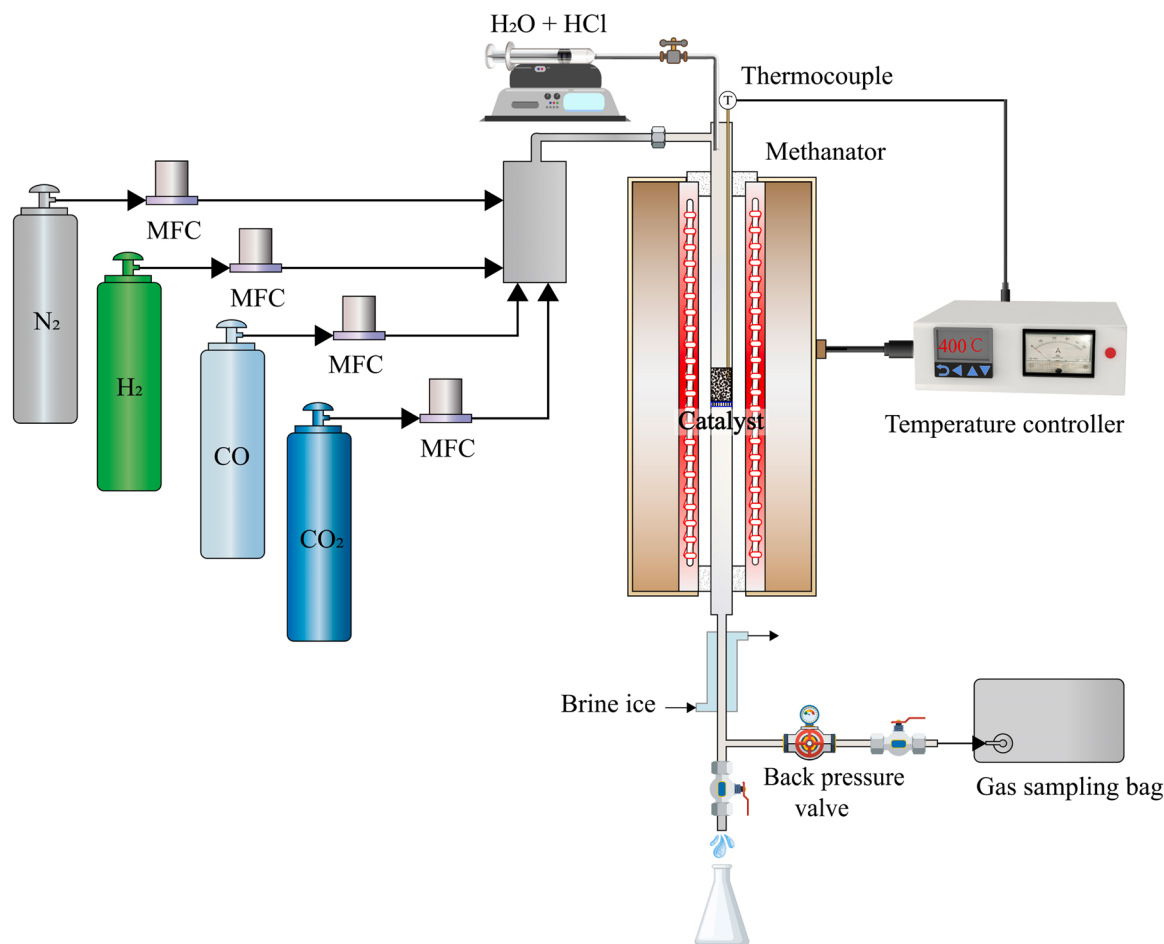


**Fig. 2.** Schematic diagram of the methanation apparatus.

the catalytic activity of Ni/MSWC, an alkali-carbon index was defined with consideration of different functional minerals and carbon content [5]:

$$\text{Alkali - carbon index} = \frac{\text{carbon content(wt\%)}}{100} \times \frac{\text{Fe}_2\text{O}_3 + \text{CaO} + \text{MgO} + \text{Na}_2\text{O} + \text{K}_2\text{O}}{\text{Cl}} \quad (6)$$

Among the ash components in the char carrier, AAEMs and Fe have higher concentrations (Table S1). They are also commonly recognized as promoters to enhance the activity of methanation catalysts by optimizing the surface alkalinity of the catalyst [6,20]. Both reuse methods of the recovered Ni illustrated in Fig. 1 can lead to the enrichment of acid-soluble minerals on the surface of the char carrier, consequently resulting in an increase in the alkali-carbon index.

#### 2.4. Analysis methods

The specific surface areas of the catalysts were determined by N<sub>2</sub> physisorption measurement with an ASAP 2460 type surface area and porosimeter system (Micromeritics, US) by employing the Brunauer–Emmett–Teller (BET) method. The powder X-ray diffraction (XRD) patterns of the catalyst were obtained by using a D8 ADVANCE X-Ray diffractometer (Bruker, Germany) with Cu K $\alpha$  radiation ( $\lambda = 0.1541$  nm). The crystallite sizes of the particles were calculated with Scherrer's equation of the NiO(200) and Ni<sup>0</sup>(111) XRD reflection [21]. The X-ray photoelectron spectroscopy (XPS) analysis was performed for both fresh and spent catalysts using an ESCALAB 250Xi type X-ray photoelectron spectrometer (Thermo Fisher, US). TG-MS analysis was

carried out by using a NETZSCH STA 449F3 type thermogravimetry (TG) coupled with a NETZSCH QMS 403 type mass spectrometry (MS). The TG system was heated from 50 °C to 700 °C with a heating rate of 10 °C/min under an argon flow of 100 mL/min. Evolved gases were detected by the MS online. The H<sub>2</sub> temperature-programmed reduction (H<sub>2</sub>-TPR) and CO<sub>2</sub> (or H<sub>2</sub>) temperature-programmed desorption (CO<sub>2</sub>/H<sub>2</sub>-TPD) measurements were conducted with an AutoChem II 2920 automated chemisorption analyzer (Micromeritics, US). The H<sub>2</sub> and CO<sub>2</sub> consumptions/releases were monitored with a thermal conductivity detector (TCD). The surface area of metallic Ni was measured using the H<sub>2</sub> pulse chemisorption method with a Micromeritics Autochem II 2920 type automated chemisorption analyzer. In situ DRIFTS experiments were employed to investigate the reaction intermediates formed/adsorbed on the surface of the catalyst, aiming to gain insights into the reaction mechanism, especially for CO<sub>2</sub> methanation, spectra of the emissions were analyzed with a Nicolet IS50 spectrometer equipped with a MCT detector of 4 cm<sup>-1</sup> spectral resolution and an average of 64 scans per spectrum. To carry out the analysis, in situ reduction of the sample was performed at 400 °C in a 10 % H<sub>2</sub>/Ar stream (50 mL/min) for 1 hour, with background spectra recorded. Then, a gas mixture of CO<sub>2</sub>/H<sub>2</sub> at a ratio of 1/4 was continuously introduced at 400 °C, and the in-situ DRIFTS spectra were collected after 20 minutes.

#### 2.5. DFT computational models

The carbon structure of MSWC is composed of at least two distinct aromatic carbon phases [22,23]: (i) an amorphous carbon phase with disordered graphene-like structures, which includes randomly arranged

aromatic rings, and (ii) a crystalline phase, which consists of fused aromatic layers packed in graphite-like layers, namely a turbostratic structure. Moreover, in addition to the insoluble macromolecular three-dimensional carbon matrix composed of these aromatic carbons, soluble organic compounds, such as polycyclic aromatic hydrocarbons, can also be present in the microporous system of the carbonaceous matrix or located within the gaps between graphene-like molecules [24–26]. Thus, a graphite platelet can be constructed as a simplified model to represent the surface of the MSWC. Moreover, it is important to note that there are different forms of defects in carbon structures, including Stone-Wales (SW) defect, single vacancy (SV) defect, and double vacancy (DV) defect [27]; and these defects have the potential to decrease the electronic stability in the vicinity of the graphene-like structures in the MSWC. As a result, the reactivity of carbon is enhanced.

In this study, a single-layer graphite with a single defect was constructed to simulate the MSWC surface, referred to as defective char (D-Char). Additionally, considering the interactions between periodic vacancy defects, the surface carbon atoms at the largest distance from the vacancy site are fixed [28], as depicted in Fig. 3(a). The three-dimensional Ni<sub>4</sub> tetrahedral structure [29] was selected to be adsorbed on the MSWC surface to form Ni<sub>4</sub>/D-Char structure, serving as the catalyst for CO methanation. This choice was made because it represents the smallest unit capable of exhibiting a three-dimensional structure for investigating metal-metal and metal-support interactions.

A 2 × 2 slab (four layers) with 192 Ni atoms was used to represent the Ni(111) surface, in which the bottom one layer of atoms was fixed, as shown in Fig. 3(b). The Ca<sub>4</sub>O<sub>4</sub> cluster model [30] as the representative of acid-soluble AAEMs in MSWC was positioned on top of the Ni(111) surface to explore the effect of CaO in MSWC on CO hydrogenation. Details of the calculations are given in the Supplementary material. The advantage of model calculation lies in its ability to provide insights into the atomic-level interactions among the active metal Ni, the carbon support, and the promoter, as well as to analyze the reaction mechanisms.

### 3. Results and discussion

#### 3.1. Deactivation effect of HCl

Fig. 4 illustrates the deactivation effect of HCl on the Ni/MSWC and the changes in structural characteristics of the catalyst. As depicted in Fig. 4(a), an increase in HCl concentration in syngas led to a gradual decline in CH<sub>4</sub> yield, along with a decrease in the catalyst's stability. The conversion rate of CO<sub>x(x=1,2)</sub> also decreased (Fig. S3(a)), suggesting catalyst poisoning. In Fig. 4(b), the XPS spectra suggest that Cl species were chemisorbed on the spent catalysts, as the peak area corresponding to Cl species increased with the rising HCl concentration in the syngas.

This proved that the enhanced adsorption of Cl species on the catalyst surface was related to catalyst poisoning. Furthermore, a higher HCl concentration in syngas corresponded to an increase in the Ni particle size during the methanation process, as illustrated in Fig. 4(c), due to the interaction of HCl with Ni nanoparticles [31]. When exposed to 200 ppm of HCl, the catalyst displayed the worst methanation performance; simultaneously, the catalyst suffered from serious Ni agglomeration, with Ni particle size increasing to 37.4 nm. Fig. 4(d) illustrates that the spent catalyst still displayed a higher specific surface area than the fresh one. This was because the char carrier was gasified by H<sub>2</sub>O produced during methanation or present in the feeding gas while Ni enhanced this gasification. The physical disintegration of the char carrier induced by carbon gasification could also significantly influence the catalytic performance. Additionally, the pore structure change caused by H<sub>2</sub>O gasification was likely to facilitate the re-dispersion of Ni particles by influencing Ni-C interactions (Fig. S3(b)), resulting in a decrease in their size from 25.7 nm of the fresh catalyst to 15.7 nm after reaction (Fig. 4(c)). To verify the feasibility of the above two Ni recovery and reuse methods, the deactivated catalyst exposed to 200 ppm of HCl was employed as a representative sample.

#### 3.2. Choice of Ni recovery method

Fig. 5 illustrates the impacts of two Ni recovery and reuse methods (Fig. 1(a) & 1(b)) on the methanation performance of Ni/MSWC catalysts. The methanation performance of R1-a was markedly inferior to that of R1-b, as evidenced by Figs. 5(a) and 5(b). This result suggested that utilization of the acidic extraction solution containing HNO<sub>3</sub> to impregnate a fresh MSWC was not a good choice, while the method demonstrated in Fig. 1(b) was more suitable for Ni recovery and reuse.

The TG-MS analysis was adopted to investigate the thermal stability of the char carriers, as illustrated in Fig. 5(c), for R1-a prepared by the method in Fig. 1(a), rich CO and CO<sub>2</sub> release was detected during the programmed heating process from 50 to 700 °C, with peaks appearing around 380 °C, but R1-b did not show similar emissions. The release of CO and CO<sub>2</sub> from HNO<sub>3</sub>-treated char indicated that HNO<sub>3</sub> solution treatment led to oxidation of the MSWC, which generated oxygen-containing functional groups [32] but carbon was consumed simultaneously. Oxygen-containing functional groups could provide anchoring sites for metal species, thereby improving metal dispersion and controlling the size of metal particles [4]. However, during the calcination and reduction pre-treatments (at 400 °C) of the catalyst and the subsequent exothermic methanation process ( $\geq 400$  °C), the high temperature could lead to the decomposition of unstable oxygen-containing complexes, resulting in Ni (or NiO) particles stripping from the char surface and its agglomeration [33]. Therefore, the thermally unstable oxygen-containing functional groups on the surface of the MSWC carrier

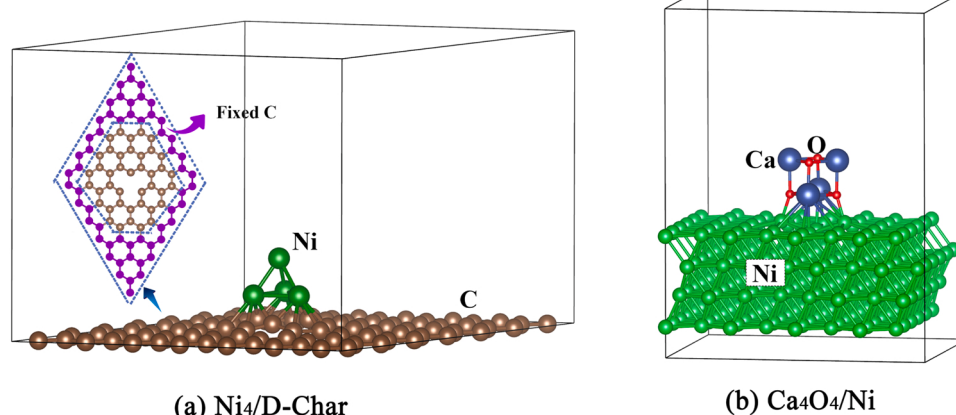
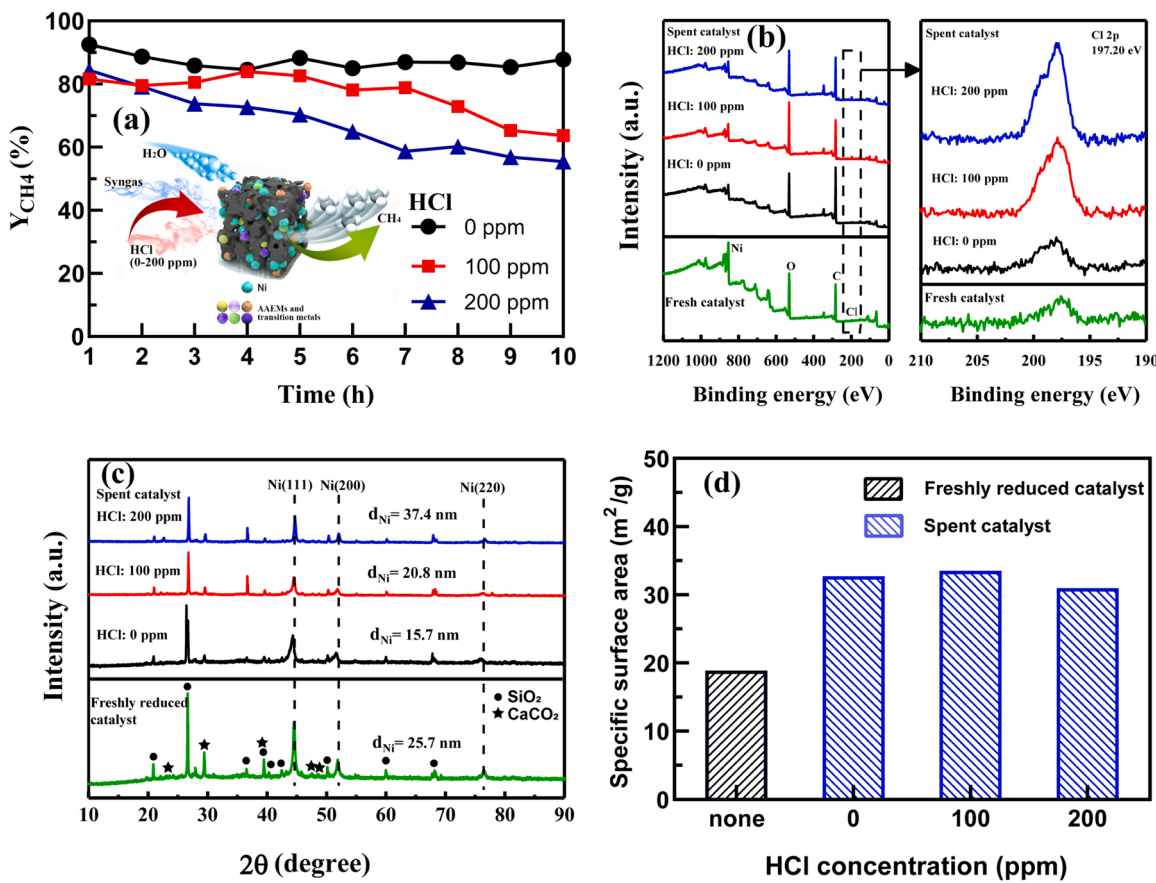


Fig. 3. The optimized slab model of the Ni<sub>4</sub>/D-Char and Ca<sub>4</sub>O<sub>4</sub>/Ni.



**Fig. 4.** Catalytic performance and structural properties of poisoned catalysts: (a) CH<sub>4</sub> yield; (b) XPS analysis; (c) XRD analysis; (d) Specific surface area.

would potentially deteriorate the dispersion of Ni particles, resulting in declined catalytic activity and stability. The average particle size of NiO for R1-a exhibited an increase from 11.3 nm of R0 to 13.8 nm after the calcination process, as shown in Fig. 5(d), proving that the oxidation of char carrier induced the agglomeration of NiO particles; while the smaller NiO size of R1-b corresponded to a higher CH<sub>4</sub> yield. On the other hand, HNO<sub>3</sub>-treated MSWC showed a higher carbon structural defect density (Fig. S4). Thus, in Fig. 5(d), the R1-a catalyst exhibited the formation of metallic Ni through carbon reduction of NiO during the calcination process due to the higher reactivity of structural defect. But the higher CH<sub>4</sub> yield of the R1-b catalyst proved the importance of the thermal stability of the char carrier. Therefore, the method shown in Fig. 1(b) was used for subsequent Ni recovery tests.

### 3.3. Performance and properties of the catalysts prepared by recovered Ni

Fig. 6 shows the methanation performance and stability of the catalysts prepared with recovered Ni after different numbers of Ni recovery cycles following the method in Fig. 1(b). Figs. 6(a)-6(c) demonstrated significant decreases in the conversion rates of CO, CO<sub>2</sub> and CO<sub>x</sub> when the cycle number reached four (R4). Correspondingly, noticeable reductions in CH<sub>4</sub> selectivity and yield could be observed (Fig. 6(d)&(e)). Importantly, the X<sub>CO2</sub> for R0 was lower than that for R1, R2, and R3, indicating that the accumulation of acid-extracted mineral impurities especially AAEMs in the Ni/MSWC catalyst due to Ni recovery enhanced the adsorption and conversion of CO<sub>2</sub>. Furthermore, in Fig. 6(f), R2 exhibited an improvement in catalytic stability compared to R0. Although R2 exhibited a more noticeable change in yield compared to R0 within the first 10 hours, the time point corresponding to the continuous decline in CH<sub>4</sub> yield for R2 was delayed. This improvement may be attributed to the presence of promoters, such as MgO and CaO

(Table S1) in the char carrier, promoting the catalyst's stability during the reaction process [34].

Characterization results of the R0 and catalysts prepared using the recovered Ni are shown in Fig. 7. H<sub>2</sub>-TPR analysis was performed to obtain information on the reducibility of the calcined catalyst (NiO/MSWC) and the metal-support interaction, as shown in Fig. 7(a). The reduction peak at temperatures below 300 °C was related to the presence of the free NiO [35], which had a higher reducibility than the adsorbed NiO. The reduction peak observed at higher temperatures was attributed to the reduction of NiO species, which was caused by the interaction between the Ni metal and the carrier. In Fig. 7(a), the peak position shifts progressively towards higher temperatures (>400 °C) as the Ni recovery cycle number increased. This suggested that the introduction of acid-soluble minerals in the MSWC during the recovery & reuse process enhanced the interaction between Ni species and the carrier. To investigate the impact of mineral addition on the surface basicity of catalysts, CO<sub>2</sub>-TPD tests were performed and the results are presented in Fig. 7(b). The increase in the temperature for CO<sub>2</sub> desorption peaks indicated the increase in the strength of basic sites. As the number of Ni recovery cycles increased, the introduction of more acid-soluble minerals enhanced the surface basicity of the catalysts. Additionally, in Fig. 7(c), the quantity of adsorbed CO<sub>2</sub> also increased. Consequently, the mineral introduction enhanced the catalysts' affinity for CO<sub>x</sub> [36]. This led to an increased CO<sub>2</sub> conversion rate for R1-R3 compared to R0, as shown in Fig. 6(b). The increased surface alkalinity of the catalyst resulting from minerals' introduction can also promote the hydrogenation conversion of CO by optimizing the local electronic structure of the active metal Ni [6]. However, this may not necessarily be favorable for the methanation of CO<sub>2</sub>. In Fig. 7(b), increased surface alkalinity caused by the enrichment of AAEMs from mineral impurities led to an increase in the density of strong basic sites

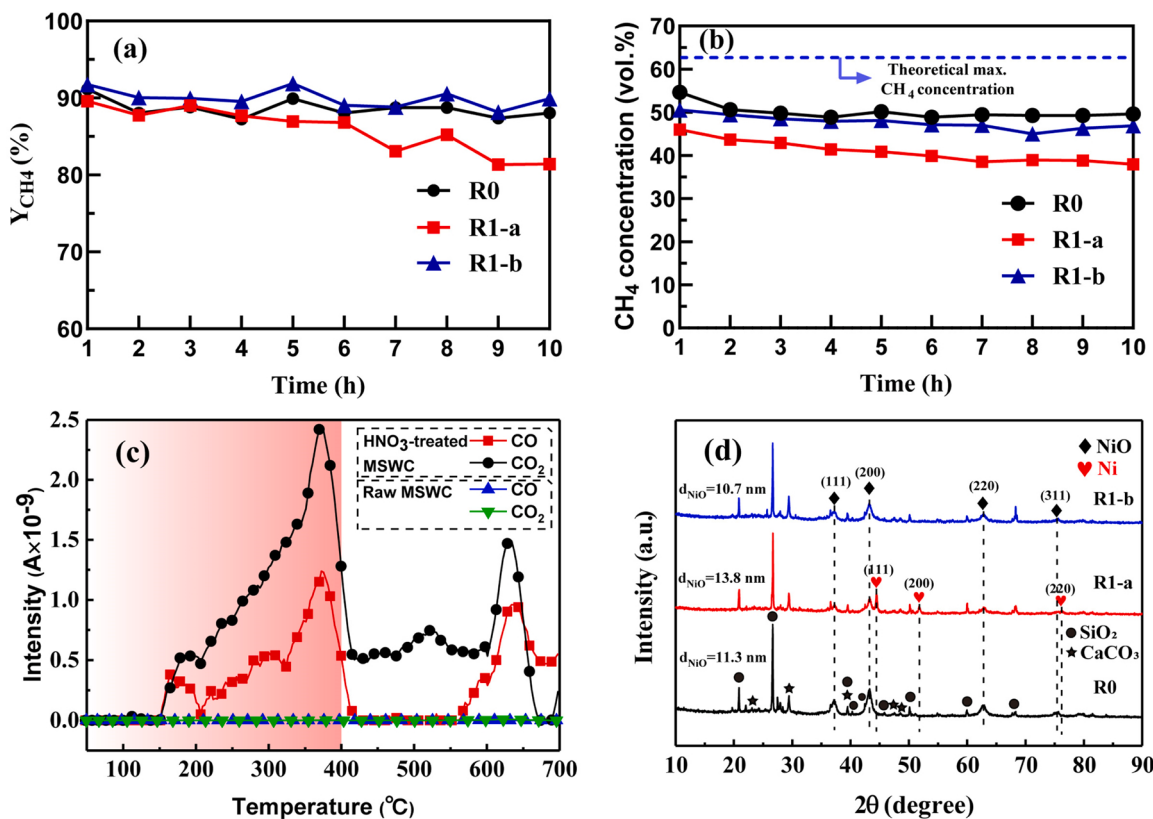


**Fig. 5.** Catalytic performance and structural properties of catalysts (at 400 °C, H<sub>2</sub>:CO:CO<sub>2</sub>:N<sub>2</sub> = 240:36:24:60): (a) CH<sub>4</sub> yield; (b) CH<sub>4</sub> concentration in the gas product; (c) TG-MS analysis; (d) XRD analysis of calcined catalysts. (R1-a and R1-b represent the catalysts obtained from the process shown in Fig. 1(a) and Fig. 1(b) respectively).

on the surface. Compared to R1-R3, when the AAEM loading was too high (as shown in R4), these strong basic sites (>600 °C) may hinder CO<sub>2</sub> methanation [37], resulting in a decrease in CO<sub>2</sub> conversion rate (Fig. 6(b)). Fig. 7(d) illustrates the H<sub>2</sub>-TPD results, providing insights into the H<sub>2</sub> adsorption capability of the catalyst surface. In Fig. 7(d), the high-temperature peaks (>400°C) were ascribed to the desorption of strongly adsorbed H<sub>2</sub> and spillover H<sub>2</sub> [38–40]. Meanwhile, Fig. 7(d) shows a shift of the hydrogen desorption peak position of R4 to the high-temperature region, compared to R0 and R2. The lower temperature peak shifts to a higher temperature suggest the enhanced adsorption ability for H<sub>2</sub> [41]. Therefore, the introduction of acid-soluble minerals on the surface of char support may enhance the adsorption of H<sub>2</sub>. This type of adsorption was difficult to be desorbed from the active sites [42, 43], and thus unfavorable for CO<sub>x</sub> methanation, due to the competitive adsorption between CO<sub>x</sub> and H<sub>2</sub> [44].

In Fig. 7(c), with an increasing number of Ni recovery cycles, there was an increase in the ash content in the Ni/MSWC catalysts due to the accumulation of minerals. Correspondingly, the specific surface area of Ni metal gradually decreased. In Fig. 7(e), the Ni/Si atomic ratios of the catalyst were provided, which were obtained from the XPS results, it can be seen that the Ni/Si ratio was significantly decreased for R4 when compared to that of R0. This indicated that the introduction of excessive minerals into the catalyst results in the coverage of Ni metal [45], leading to a decrease in the surface area of the Ni particles. Consequently, the catalytic activity of R4 for methanation was decreased.

Fig. 7(f) showed the correlation between the mass ratio of acid-soluble inorganic species to Ni, abbreviated as the Al/Ni ratio, in the catalysts prepared using recovered Ni, and the corresponding average CH<sub>4</sub> yield. It can be observed that there was a remarkable decrease in CH<sub>4</sub> yield when the Al/Ni ratio was greater than 3. This clearly demonstrated the negative impact of an excess of acid-soluble minerals in the carrier on the catalyst's activity, such as excessive alkalinity and

coverage of active sites. In Fig. 7(g), the analysis of pore structure revealed that when the Al/Ni ratio exceeded 3, the specific surface area of the catalyst significantly decreased, while the average pore size appreciably increased. This indicated that the introduction of excess minerals into the catalyst after undergoing multiple Ni recovery and reuse cycles also caused changes in the catalyst's pore structures, possibly due to pore blockage or the increased ash content decreasing the mass share of the carbon in the catalyst. Additionally, Fig. 7(g) also shows that the specific surface area of R1 was greater than that of R0, indicating a potential activation effect on the char carrier caused by the proper amount of acid-soluble minerals' introduction.

To understand the impact of char composition on the recovery potential of spent char-based catalysts, in Fig. 7(h), the alkali-carbon index (Eq.(6)) associated with char composition was adopted. Based on the ash composition of the catalysts prepared using recovered Ni from different recovery cycles, their alkali-carbon indexes were obtained (Table S1). Compared to the results of previous research [5], where different chars were used as carriers to support active metal Ni, the catalysts using recycled Ni (together with the acid-soluble minerals) in this research showed higher alkali-carbon indexes. It can be also seen that a satisfactory correlation between the alkali-carbon index and methanation activity can be identified although the char sources were different. After multiple Ni recovery cycles the alkali-carbon index gradually increased due to the accumulation of AAEM and Fe-containing minerals. However, the methanation activity remained stable for R0-R3, until the alkali-carbon index reached more than 29 for R4, at which point a noticeable decline in the average CH<sub>4</sub> yield was observed. Therefore, the alkali-carbon index can serve as a useful indicator for determining the optimal number of nickel recovery cycles from char-based catalysts. Moreover, the analysis of the alkali-carbon index offers insights into selecting suitable char carriers when preparing char-supported Ni catalysts. A value of around 20 indicated enhanced activity, although more

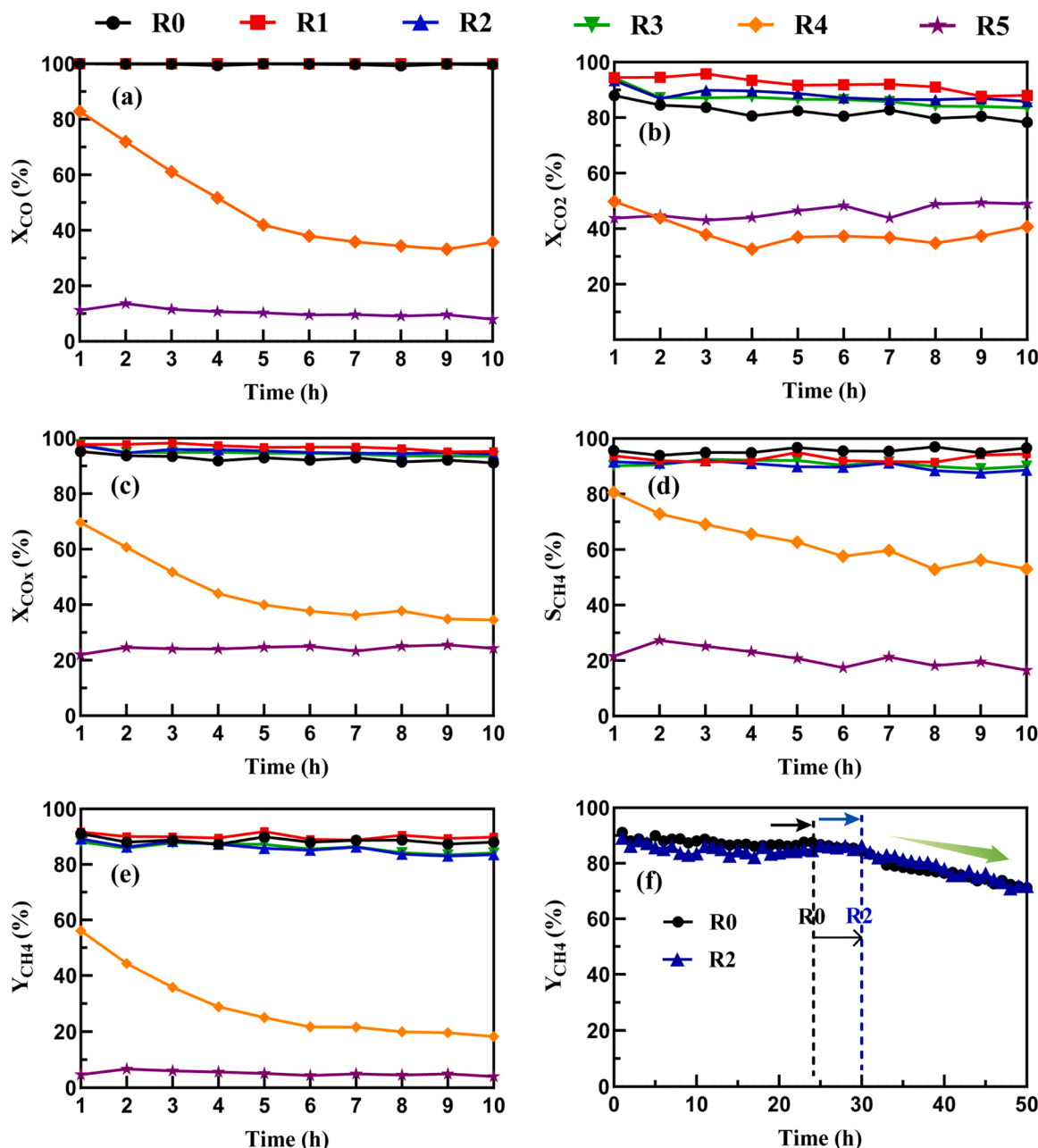


**Fig. 6.** Catalytic performance of catalysts (at 400 °C, H<sub>2</sub>:CO:CO<sub>2</sub>:N<sub>2</sub> = 240:36:24:60): (a) CO conversion; (b) CO<sub>2</sub> conversion; (c) CO<sub>x</sub> conversion; (d) CH<sub>4</sub> selectivity; (e) CH<sub>4</sub> yield; (f) stability test.

chars should be assessed to verify the valid range of this index. In addition, for R1-a and R1-b, their index values were almost the same, varying only slightly due to carbon oxidation of R1-a. In fact, the different methods for preparing catalysts caused the difference in performance. The index was not the cause of the difference in catalyst performance. The results also indicated that char carriers with high AAEM content may be not suitable for Ni recovery using the method in Fig. 1(b), and chars of lower ash content are more conducive to Ni recovery and reuse.

#### 3.4. Potential interactions between char components and Ni

Fig. 8 demonstrates the influence of the presence of vacancy sites (SV) in the carbon structure on the adsorption energy of nickel clusters. The results showed that the presence of defects in the carbon structure significantly promoted the adsorption of nickel clusters, with the

adsorption energy increased from 2.53 to 6.59 eV. Additionally, Bader charge analysis revealed that the electronic transfer between Ni clusters and the carbon structure was enhanced, leading to a notable increase in the Ni-C interaction. The enhanced Ni-C interaction surrounding the vacancy site hindered the diffusion of Ni atoms and the formation of larger Ni clusters over the carbon substrate. Therefore, the presence of defects in the carbon structure facilitated the anchoring of Ni particles, thereby enhancing catalytic stability. In Fig. 5(c), HNO<sub>3</sub> treatment resulted in the formation of a large number of oxygen-containing functional groups on the surface of char, which also improved the carbon defect sites of the R1-a catalyst (Fig. S4). However, in Fig. 5(d), the size of the Ni particles corresponding to R1-a was still slightly larger than that of R0. This indicated that during the impregnation process, a significant interaction occurred between the active metal precursor and oxygen-containing functional groups, rather than carbon structural defects. During the thermal pretreatment of the catalyst, the

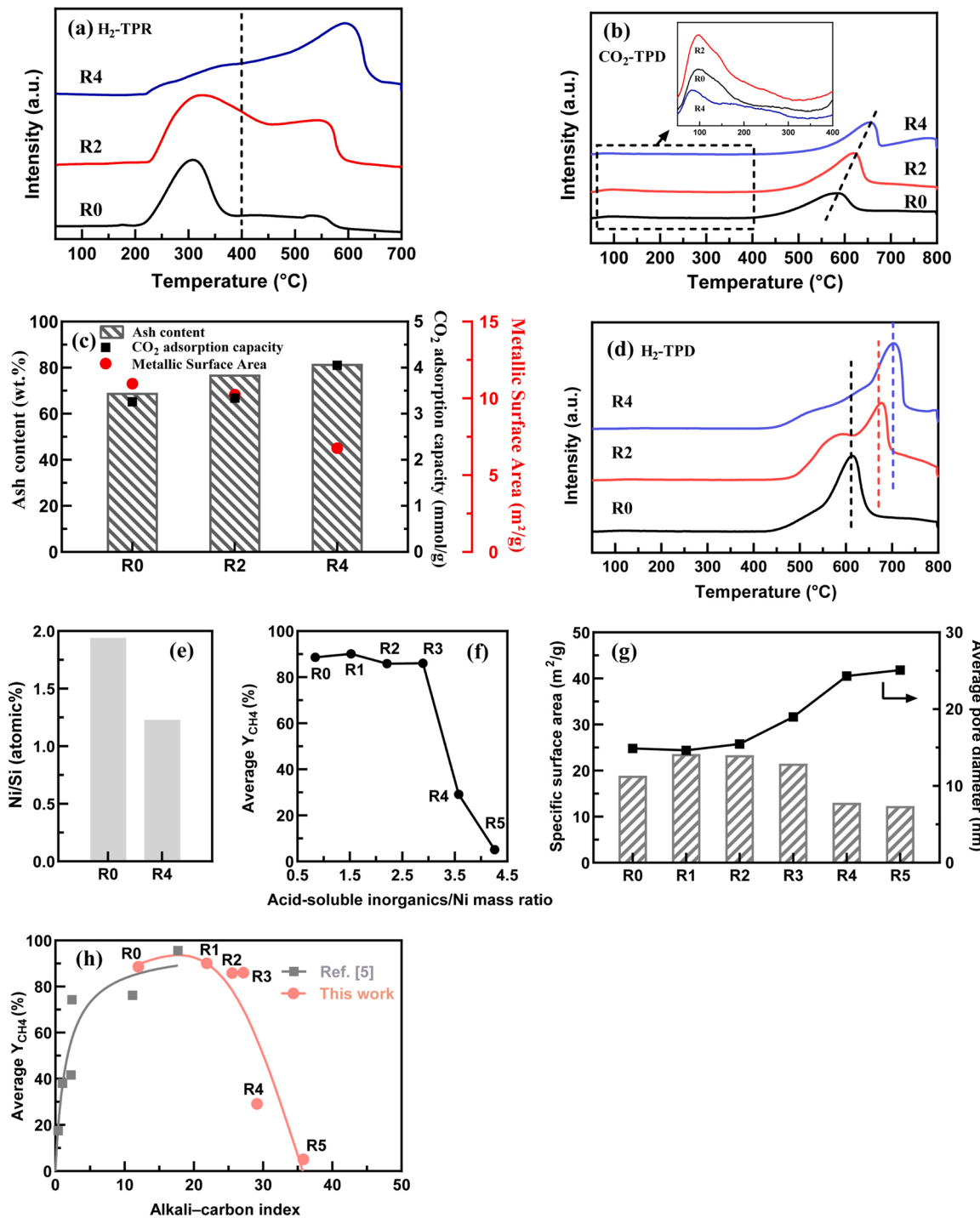


**Fig. 7.** Surface characteristics of the original catalyst and the catalyst prepared using the recovered Ni: (a)  $H_2$ -TPR; (b)  $CO_2$ -TPD; (c) Ash content,  $CO_2$  adsorption capacity and Metallic surface area; (d)  $H_2$ -TPD; (e) Ni/Si atomic ratio; (f) effect of Al/Ni mass ratio on  $CH_4$  yield; (g) pore structure of catalysts; (h) Correlation between catalytic performance and char properties.

decomposition of oxygen-containing functional groups was the main reason for the increase in Ni particle size.

AAEMs are widely present in MSWC (Table S1); thus, in this study, the AAEM species in MSWC were still retained in the acid-extraction solution and recovered, as shown in Fig. 1(b). Therefore, in this context, CaO and KCl were selected as representative acid-soluble and water-soluble species of AAEMs for mechanism investigation and they interact independently with the Ni surface without synergistic effects (Fig. S5). Fig. 9(a) shows the differential charge density iso-surface contours of  $Ca_4O_4/Ni$  and  $K_4Cl_4/Ni$ . In comparison to  $K_4Cl_4/Ni$ , there

was a more noticeable charge transfer between  $Ca_4O_4$  and Ni surface. Meanwhile, when the  $Ca_4O_4$  cluster was present on the Ni surface,  $E_{ads}(CO)$  increased from 2.01 to 2.49 eV, which was higher than that of  $K_4Cl_4/Ni$  (2.31 eV). This can be attributed to the more obvious electron transfer toward metal Ni, which increased the back-donation of the metal electrons into the  $2\pi^*$  antibonding orbitals of adsorbed CO and strengthened the metal-CO bond [46], leading to improved CO methanation. Similarly, elevated electron density via reactions involving electron transfer can also facilitate the absorption and activation of molecules of  $CO_2$  [47]. Additionally, the CaO surface also exhibited  $CO_2$

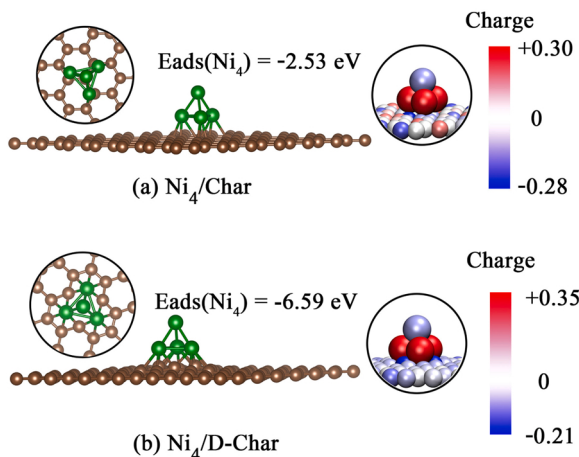


**Fig. 8.** The optimized adsorption configurations of Ni on the carbon substrate and Bader charge analysis. (The positive/negative charge indicates the electron loss/gain from the Ni atoms; "Char" and "D-char" respectively represent carbon substrates without any defects and with a single vacancy defect).

adsorption [48]. As shown in Fig. 6(b), the CO<sub>2</sub> conversion rates for R1-R3 were considerably greater than that of R0. Therefore, the presence of basic oxides on the Ni surface can enhance the adsorption of reactant molecules and improve the catalytic activity for methanation by improving the electronic structure of the active metal surface.

Moreover, as shown in Fig. 9(a), the electron-donating ability of the K<sub>4</sub>Cl<sub>4</sub> cluster was notably weaker compared to that of the Ca<sub>4</sub>O<sub>4</sub> cluster, which was inconsistent with the higher electron-donating ability typically observed in alkali metals. This indicated that the presence of alkali metals in different forms can also impact the catalytic performance. The role of AAEMs as electron promoters was enhanced when they were present in oxide form. Previous studies have reported the frequent utilization of AAEMs as promoters in the preparation of methanation catalysts, where nitrates were commonly employed as their metal precursors [45,49,50]. The calcination process resulted in the decomposition of these nitrates into AAEM oxides, which then acted as the active promoters. Therefore, the utilization of nitric acid as a solvent for metal recovery enabled the conversion of the acid-soluble inorganics in MSWC into nitrates, thereby enhancing their role as electron promoters. In Fig. 9(a), compared with the K<sub>4</sub>Cl<sub>4</sub> cluster, a metal atom of the Ca<sub>4</sub>O<sub>4</sub>

cluster located near the Ni surface exhibited a more significant change in electron loss before and after the adsorption of the CO molecule, decreasing from 1.22 to 1.09 eV, suggesting that there was an interaction between the Ca atom in the Ca<sub>4</sub>O<sub>4</sub> cluster and the O atom in CO<sub>ad</sub>, which can also explain the increased CO adsorption capability of the Ca<sub>4</sub>O<sub>4</sub>/Ni structure. On the other hand, although the presence of inherent inorganics (such as AAEMs) in the MSWC can modify the local electron density of transition metal Ni, thereby enhancing the methanation activity of the MSWC-supported Ni catalyst, the repeated recovery process inevitably led to the accumulation of mineral species on the catalyst's surface. This accumulation covered the active sites (Fig. 7(e)) and suppressed methanation reactions, as depicted in Fig. 9(b). The Ni in the spent catalyst that cannot be further recovered by acid extraction can still be recovered following regular methods using hydrometallurgical methods [51].

### 3.5. Methanation mechanism

Fig. 10 displayed the potential energy diagram depicting the optimal pathway for CO hydrogenation to CH<sub>4</sub> over Ni<sub>4</sub>-D-Char. The stable configurations of possible species involved in the CO hydrogenation are given in Fig. S6. The mechanism for CO methanation can be divided into two types [6]: (1) associative methanation and (2) dissociative methanation. Accordingly, the initial CO reaction can proceed through two distinct pathways: direct dissociation of CO into carbon and oxygen atoms, or hydrogenation of CO to form carbon-hydroxyl (COH<sub>ad</sub>) or formyl (CHO<sub>ad</sub>) species. In Fig. 10(a), the activation energy barriers for CHO and COH formation were 1.38 eV and 1.93 eV, respectively, which were lower compared to that of direct CO dissociation. Consequently, CHO served as the primary intermediate in CO hydrogenation over Ni<sub>4</sub>-D-Char, with hydrogen-assisted CO dissociation being the dominant pathway for CO methanation on Ni. The subsequent optimal reaction routes for the CHO intermediates are shown in Fig. 10(b-d), it can be seen that the optimal pathway for CO hydrogenation on Ni was: CO + 6 H → CHO + 5 H → CH<sub>2</sub>O + 4 H → CH<sub>3</sub>O + 3 H → CH<sub>3</sub> + H + H<sub>2</sub>O → CH<sub>4</sub> + H<sub>2</sub>O.

Moreover, in situ DRIFT tests were conducted to understand the key surface species on the catalyst surface during the hydrogenation process of CO<sub>2</sub> in syngas, as shown in Fig. 11(a), it showed obvious absorption peaks in two spectral band regions. The band in the region of 3500–3800 cm<sup>-1</sup> can be attributed to \*OH species [52,53], and the bands at ~2210 cm<sup>-1</sup> and ~2270 cm<sup>-1</sup> correspond to gaseous \*CO and

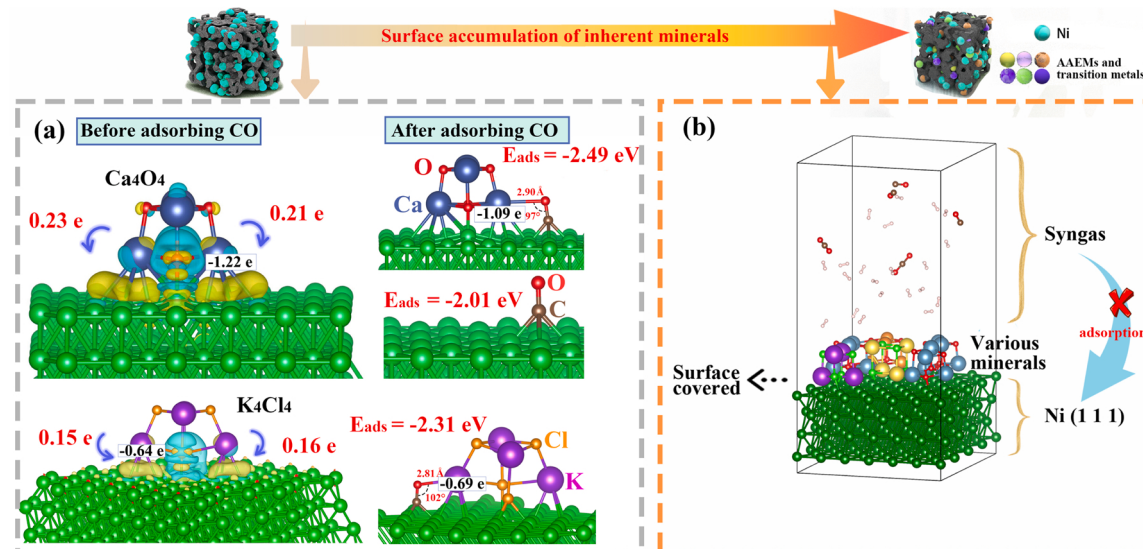


**Fig. 9.** Interactions between minerals and Ni in the catalyst: (a) Differential charge density iso-surface contours for Ca<sub>4</sub>O<sub>4</sub>/Ni and K<sub>4</sub>Cl<sub>4</sub>/Ni (The cyan and yellow contours indicate electron density decrease and increase by 0.003 e/Å<sup>3</sup>, respectively); (b) Schematic diagram for the Ni surface covered by accumulated minerals.

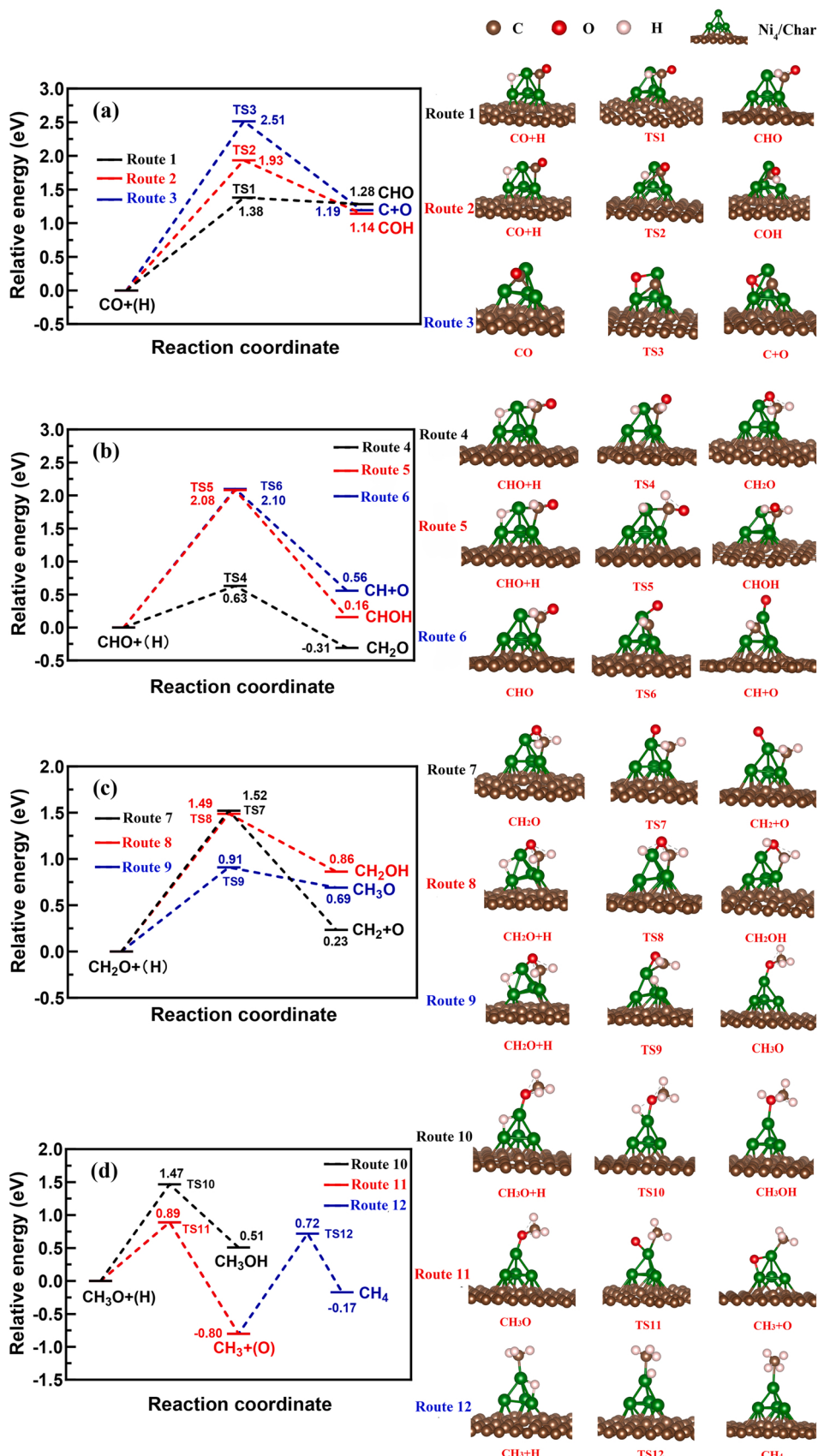
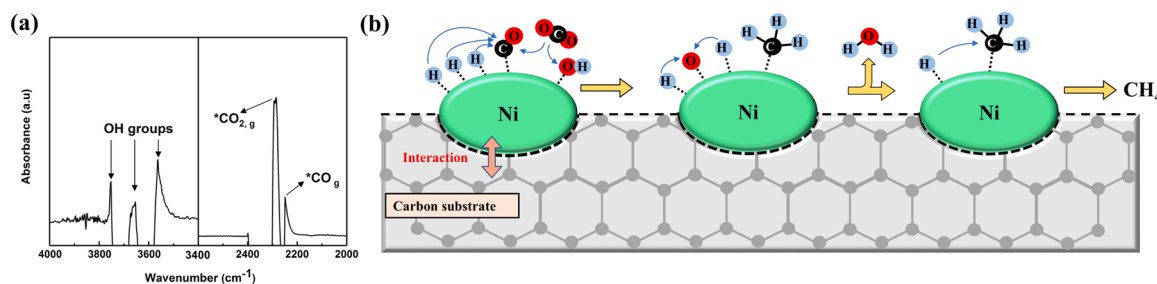


Fig. 10. Reaction pathways of (a) CHO, (b) CH<sub>2</sub>O, (c) CH<sub>3</sub>O, and (d) CH<sub>4</sub> formations in CO hydrogenation.



**Fig. 11.** (a) In situ DRIFTS spectra under  $\text{CO}_2$  methanation condition; (b) Potential reaction pathways for  $\text{CO}_2$  hydrogenation to  $\text{CH}_4$ .

gaseous  $^*\text{CO}_2$  species, respectively [53,54]. The presence of CO in the syngas can inhibit  $\text{CO}_2$  methanation, suggesting that the adsorption of  $\text{CO}_2$  on the active sites is the rate-limiting step for the overall process of  $\text{CO}_2$  methanation [55]. It can be inferred that CO did not affect the hydrogenation pathway of  $\text{CO}_2$ . Therefore, in this study,  $\text{CO}_2$  in the syngas was initially hydrogenated to gaseous  $^*\text{CO}$  species, followed by an associative CO methanation process, as shown in Fig. 11(b). It can be considered that  $^*\text{CO}$  was a key adsorbed intermediate in the CO& $\text{CO}_2$  co-methanation process, which was consistent with the previous reports [55,56]. However, unlike the traditional carrier that requires promoter modification, the mineral impurities in the char carrier can serve as a natural promoter, enhancing the methanation performance of the char-supported Ni catalyst. During the methanation process, the inherent AAEMs in the char carrier promoted the adsorption and activation of  $\text{H}_2\text{O}$ , generating active hydroxyl groups [57], which may induce the conversion of  $\text{CO}_2$  in the syngas to CO. Furthermore, these AAEMs also improved the local electron density of the active metal Ni, consequently facilitating an enhancement in the catalyst activity.

#### 4. Conclusions

In this study, a simple acid-assisted Ni recovery from the spent Ni/MSWC catalysts and its reuse for preparing new catalysts was proposed, aiming to recover nickel resources, as well as being an effective approach to regularly change the content acid-soluble minerals in the char carrier. The performance evolution of the catalysts prepared using this method was discussed, along with its correlation with the char characteristics, so to assess the reliability of the different chars as catalyst carriers. Additionally, the hydrogenation mechanism of CO& $\text{CO}_2$  over Ni/MSWC and the interaction between Ni and char in char-based catalysts were explored. The conclusions are as follows:

(1) A "oxidization of the spent catalyst - acid-extraction - evaporation - reuse for impregnation" process was recommended to recover Ni from the spent catalyst and avoid damage to the char structure caused by  $\text{HNO}_3$  in the extraction solution. The catalysts after being prepared using the recovered Ni showed similar methanation activity to the original catalyst after three cycles of Ni recovery and reuse.

(2) Repeated Ni recovery and reuse could lead to the enrichment of acid-soluble mineral species from char carrier on the catalyst surface, which in turn affected its surface chemical adsorption properties, changed surface alkalinity, and covered the active sites, thereby inducing deactivation behavior. This resulted in the methanation activity of the catalyst obtained in the fourth recovery cycle showing a significant drop.

(3) The surface structural defects of char carriers contributed to the anchoring of Ni particles, which could potentially improve catalytic stability. Active mineral impurities (e.g., AAEMs) in waste-derived char can be used as natural promoters to promote the adsorption and activation of CO& $\text{CO}_2$  by activating intermediate products and optimizing the electron density of Ni particles, thereby forming the key intermediate  $^*\text{CO}$ , followed by H-assisted dissociation pathways.

(4) The alkali-carbon index was utilized to evaluate the properties of char as a catalyst carrier. The increased alkali-carbon index, resulting

from the enrichment of acid-soluble minerals, enhanced  $\text{CO}_x$  adsorption within an appropriate range. However, a higher alkali-carbon index, such as 29, would detrimentally impact the activity of char-based catalysts. The implications of the alkali-carbon index include selecting suitable char carriers and determining the optimal number of acid-assisted Ni recoveries for a specific spent catalyst.

#### CRediT authorship contribution statement

**Zhenfei Mei:** Writing – original draft, Methodology, Investigation, Formal analysis, Data curation. **Hongquan Zhou:** Validation, Resources, Conceptualization. **Shaoheng Ge:** Validation, Resources, Conceptualization. **Yuheng Feng:** Validation, Resources, Conceptualization. **Dezhen Chen:** Writing – review & editing, Supervision, Resources, Project administration, Methodology, Funding acquisition, Formal analysis, Data curation, Conceptualization.

#### Declaration of Competing Interest

The authors declare that they have no known competing financial interests or personal relationships that could have appeared to influence the work reported in this paper.

#### Data availability

Data will be made available on request.

#### Acknowledgement

This research work was financially supported by Shanghai Municipal Science and Technology Commission (Grant No. 20230712900) and (Grant No. 22dz1208200).

#### Appendix A. Supporting information

Supplementary data associated with this article can be found in the online version at doi:10.1016/j.apcatb.2024.124234.

#### References

- [1] D. Chen, L. Yin, H. Wang, P. He, Pyrolysis technologies for municipal solid waste: a review, *Waste Manag* 34 (2014) 2466–2486, <https://doi.org/10.1016/j.wasman.2014.08.004>.
- [2] Z. Mei, D. Chen, K. Qian, L. Yin, L. Hong, Producing methane from dry municipal solid wastes: a complete roadmap and the influence of char catalyst, *Energy* 290 (2024) 130180, <https://doi.org/10.1016/j.energy.2023.130180>.
- [3] A.C. Ghogia, A. Nzhou, P. Serp, K. Soulantica, D. Pham Minh, Cobalt catalysts on carbon-based materials for Fischer-Tropsch synthesis: a review, *Appl. Catal. Gen.* 609 (2021) 117906, <https://doi.org/10.1016/j.apcata.2020.117906>.
- [4] Y. Yang, K. Chiang, N. Burke, Porous carbon-supported catalysts for energy and environmental applications: a short review, *Catal. Today* 178 (2011) 197–205, <https://doi.org/10.1016/j.cattod.2011.08.028>.
- [5] Z. Mei, D. Chen, G. Yuan, R. Zhang, Waste-derived chars as methanation catalyst support: role of inorganics in the char and its guide to catalyst design, *Fuel* 349 (2023) 128574, <https://doi.org/10.1016/j.fuel.2023.128574>.
- [6] I. Hussain, A.A. Jalil, N.S. Hassan, M. Farooq, M.A. Mujtaba, M.Y.S. Hamid, H.M. A. Sharif, W. Nabgan, M.A.H. Aziz, A. Owgi, Contemporary thrust and emerging

- prospects of catalytic systems for substitute natural gas production by CO methanation, *Fuel* (2021) 122604, <https://doi.org/10.1016/j.fuel.2021.122604>.
- [7] L.P.L. Gonçalves, J.P.S. Sousa, O.S.G.P. Soares, O. Bondarchuk, O.I. Lebedev, Y. V. Kolen'ko, M.F.R. Pereira, The role of surface properties in CO<sub>2</sub> methanation over carbon-supported Ni catalysts and their promotion by Fe, *Catal. Sci. Technol.* 10 (2020) 7217–7225, <https://doi.org/10.1039/D0CY01254H>.
- [8] M. Marafi, A. Stanislaus, Waste catalyst utilization: extraction of valuable metals from spent hydroprocessing catalysts by ultrasonic-assisted leaching with acids, *Ind. Eng. Chem. Res.* 50 (2011) 9495–9501, <https://doi.org/10.1021/ie200789u>.
- [9] N.M. Al-Mansi, N.M. Abdel Monem, Recovery of nickel oxide from spent catalyst, *Waste Manag.* 22 (2002) 85–90, [https://doi.org/10.1016/S0956-053X\(01\)00024-1](https://doi.org/10.1016/S0956-053X(01)00024-1).
- [10] R. Oza, N. Shah, S. Patel, Recovery of nickel from spent catalysts using ultrasonication-assisted leaching, *J. Chem. Technol. Biotechnol.* 86 (2011) 1276–1281, <https://doi.org/10.1002/jctb.2649>.
- [11] C. Mebrahtu, S. Perathoner, G. Giorgiani, S. Chen, G. Centi, F. Krebs, R. Palkovits, S. Abate, Deactivation mechanism of hydrotalcite-derived Ni-AlO<sub>x</sub> catalysts during low-temperature CO<sub>2</sub> methanation via Ni-hydroxide formation and the role of Fe in limiting this effect, *Catal. Sci. Technol.* 9 (2019) 4023–4035, <https://doi.org/10.1039/C9CY00744J>.
- [12] J. Ren, J.-P. Cao, F.-L. Yang, Y.-L. Liu, W. Tang, X.-Y. Zhao, Understandings of catalyst deactivation and regeneration during biomass tar reforming: a crucial review, *ACS Sustain. Chem. Eng.* 9 (2021) 17186–17206, <https://doi.org/10.1021/acssuschemeng.1c07483>.
- [13] D.K. Binte Mohamed, A. Veksha, T.-T. Lim, G. Lisak, Hydrogen bromide in syngas: effects on tar reforming, water gas-shift activities and sintering of Ni-based catalysts, *Appl. Catal. B Environ.* 280 (2021) 119435, <https://doi.org/10.1016/j.apcatb.2020.119435>.
- [14] I.S. Pieta, W.S. Epling, A. Kazmierczuk, P. Lisowski, R. Nowakowski, E. M. Serwicka, Waste into Fuel—Catalyst and process development for MSW valorisation, *Catalysts* 8 (2018) 113, <https://doi.org/10.3390/catal8030113>.
- [15] C. Berrueco, J. Recari, S. Abelló, X. Farriol, D. Montané, Experimental investigation of solid recovered fuel (SRF) gasification: Effect of temperature and equivalence ratio on process performance and release of minor contaminants, *Energy Fuels* 29 (2015) 7419–7427, <https://doi.org/10.1021/acs.energyfuels.5b02032>.
- [16] M. Chen, D. Chen, U. Arena, Y. Feng, H. Yu, Treatment of volatile compounds from municipal solid waste pyrolysis to obtain high quality syngas: effect of various scrubbing devices, *Energy Fuels* 31 (2017) 13682–13691, <https://doi.org/10.1021/acs.energyfuels.7b02388>.
- [17] A.R. Sheik, M.K. Ghosh, K. Sanjay, T. Subbaiah, B.K. Mishra, Dissolution kinetics of nickel from spent catalyst in nitric acid medium, *J. Taiwan Inst. Chem. Eng.* 44 (2013) 34–39, <https://doi.org/10.1016/j.jtice.2012.08.003>.
- [18] H.-H. Tseng, M.-Y. Wey, Effects of acid treatments of activated carbon on its physiochemical structure as a support for copper oxide in DeSO<sub>2</sub> reaction catalysts, *Chemosphere* 62 (2006) 756–766, <https://doi.org/10.1016/j.chemosphere.2005.04.077>.
- [19] J. Silvestre-Albero, M. Martínez-Escandell, J. Narciso, A. Sepúlveda-Escribano, M. Molina-Sabio, The scientific impact of Francisco Rodríguez-Reinoso in carbon research and beyond, *Carbon* 179 (2021) 275–287, <https://doi.org/10.1016/j.carbon.2021.04.015>.
- [20] M. González-Castaño, J. González-Arias, L.F. Bobadilla, E. Ruíz-López, J. A. Odriozola, H. Arellano-García, *In-situ* DRIFTS steady-state study of CO<sub>2</sub> and CO methanation over Ni-promoted catalysts, *Fuel* 338 (2023) 127241, <https://doi.org/10.1016/j.fuel.2022.127241>.
- [21] J. Ren, J.-P. Cao, F.-L. Yang, X.-Y. Zhao, W. Tang, X. Cui, Q. Chen, X.-Y. Wei, Layered uniformly delocalized electronic structure of carbon supported Ni catalyst for catalytic reforming of toluene and biomass tar, *Energy Convers. Manag.* 183 (2019) 182–192, <https://doi.org/10.1016/j.enconman.2018.12.093>.
- [22] D.B. Wiedemeier, S. Abiven, W.C. Hockaday, M. Keiluweit, M. Kleber, C. A. Masiello, A.V. McBeath, P.S. Nico, L.A. Pyle, M.P.W. Schneider, R.J. Smernik, G. L.B. Wiesenberg, M.W.I. Schmidt, Aromaticity and degree of aromatic condensation of char, *Org. Geochem.* 78 (2015) 135–143, <https://doi.org/10.1016/j.orggeochem.2014.10.002>.
- [23] K. Zhang, P. Sun, M.C.A.S. Faye, Y. Zhang, Characterization of biochar derived from rice husks and its potential in chlorobenzene degradation, *Carbon* 130 (2018) 730–740, <https://doi.org/10.1016/j.carbon.2018.01.036>.
- [24] X. Xiao, B. Chen, A direct observation of the fine aromatic clusters and molecular structures of biochars, *Environ. Sci. Technol.* 51 (2017) 5473–5482, <https://doi.org/10.1021/acs.est.6b06300>.
- [25] M. Keiluweit, M. Kleber, M.A. Sparrow, B.R.T. Simoneit, F.G. Prahl, Solvent-extractable polycyclic aromatic hydrocarbons in biochar: Influence of pyrolysis temperature and feedstock, *Environ. Sci. Technol.* 46 (2012) 9333–9341, <https://doi.org/10.1021/es302125k>.
- [26] Z. Lei, D. Yang, Y. Zhang, P. Cui, Constructions of coal and char molecular models based on the molecular simulation technology, *J. Fuel Chem. Technol.* 45 (2017) 769–779, [https://doi.org/10.1016/S1872-5813\(17\)30038-5](https://doi.org/10.1016/S1872-5813(17)30038-5).
- [27] D.P. Serrano, J.A. Botas, J.L.G. Fierro, R. Guil-López, P. Pizarro, G. Gómez, Hydrogen production by methane decomposition: origin of the catalytic activity of carbon materials, *Fuel* 89 (2010) 1241–1248, <https://doi.org/10.1016/j.fuel.2009.11.030>.
- [28] L. Fan, L. Ling, B. Wang, R. Zhang, The adsorption of mercury species and catalytic oxidation of Hg<sup>0</sup> on the metal-loaded activated carbon, *Appl. Catal. Gen.* 520 (2016) 13–23, <https://doi.org/10.1016/j.apcata.2016.03.036>.
- [29] Y. Wang, Y. Su, M. Zhu, L. Kang, Mechanism of CO methanation on the Ni<sub>4</sub>/γ-Al<sub>2</sub>O<sub>3</sub> and Ni<sub>3</sub>Fe/γ-Al<sub>2</sub>O<sub>3</sub> catalysts: a density functional theory study, *Int. J. Hydron. Energy* 40 (2015) 8864–8876, <https://doi.org/10.1016/j.ijhydene.2015.05.002>.
- [30] X. Ma, Y. Li, W. Zhang, Z. Wang, J. Zhao, DFT study of CO<sub>2</sub> adsorption across a CaO/Ca<sub>12</sub>Al<sub>14</sub>O<sub>33</sub> sorbent in the presence of H<sub>2</sub>O under calcium looping conditions, *Chem. Eng. J.* 370 (2019) 10–18, <https://doi.org/10.1016/j.cej.2019.03.176>.
- [31] A. Veksha, A. Giannis, W.-D. Oh, V.W.-C. Chang, G. Lisak, T.-T. Lim, Catalytic activities and resistance to HCl poisoning of Ni-based catalysts during steam reforming of naphthalene, *Appl. Catal. Gen.* 557 (2018) 25–38, <https://doi.org/10.1016/j.apcata.2018.03.005>.
- [32] N.B. Klinghoffer, M.J. Castaldi, A. Nzihou, Influence of char composition and inorganics on catalytic activity of char from biomass gasification, *Fuel* 157 (2015) 37–47, <https://doi.org/10.1016/j.fuel.2015.04.036>.
- [33] S. Wang, G.Q. (Max) Lu, Effects of oxide promoters on metal dispersion and metal–support interactions in Ni catalysts supported on activated carbon, *Ind. Eng. Chem. Res.* 36 (1997) 5103–5109, <https://doi.org/10.1021/ie9703604>.
- [34] H. Wan, Y. He, Q. Su, L. Liu, X. Cui, Slag-based geopolymers microspheres as a support for CO<sub>2</sub> methanation, *Fuel* 319 (2022) 123627, <https://doi.org/10.1016/j.fuel.2022.123627>.
- [35] W. Wang, W. Chu, N. Wang, W. Yang, C. Jiang, Mesoporous nickel catalyst supported on multi-walled carbon nanotubes for carbon dioxide methanation, *Int. J. Hydron. Energy* 41 (2016) 967–975, <https://doi.org/10.1016/j.ijhydene.2015.11.133>.
- [36] L. He, Q. Lin, Y. Liu, Y. Huang, Unique catalysis of Ni-Al hydrotalcite derived catalyst in CO<sub>2</sub> methanation: cooperative effect between Ni nanoparticles and a basic support, *J. Energy Chem.* 23 (2014) 587–592, [https://doi.org/10.1016/S2095-4956\(14\)60144-3](https://doi.org/10.1016/S2095-4956(14)60144-3).
- [37] K.N. Ahmad, W.N.R. Wan Isahak, M.I. Rosli, M.R. Yusop, M.B. Kassim, M. A. Yarmo, Rare earth metal doped nickel catalysts supported on exfoliated graphitic carbon nitride for highly selective CO and CO<sub>2</sub> methanation, *Appl. Surf. Sci.* 571 (2022) 151321, <https://doi.org/10.1016/j.apsusc.2021.151321>.
- [38] Y. Han, Y. Quan, J. Zhao, J. Ren, Promotion effect by Mg on the catalytic behavior of MgNi/WO<sub>3</sub> in the CO methanation, *Int. J. Hydron. Energy* 45 (2020) 29917–29928, <https://doi.org/10.1016/j.ijhydene.2020.08.121>.
- [39] M. Mihet, M. Dan, L. Barbu-Tudoran, M.D. Lazar, CO<sub>2</sub> methanation using multimodal Ni/SiO<sub>2</sub> catalysts: effect of support modification by MgO, CeO<sub>2</sub>, and La<sub>2</sub>O<sub>3</sub>, *Catalysts* 11 (2021) 443, <https://doi.org/10.3390/catal11040443>.
- [40] M. Zieliński, R. Wojciechak, S. Montevederi, M. Mercy, M.M. Bettahar, Hydrogen storage in nickel catalysts supported on activated carbon, *Int. J. Hydron. Energy* 32 (2007) 1024–1032, <https://doi.org/10.1016/j.ijhydene.2006.07.004>.
- [41] Y. Wang, R. Wu, Y. Zhao, Effect of ZrO<sub>2</sub> promoter on structure and catalytic activity of the Ni/SiO<sub>2</sub> catalyst for CO methanation in hydrogen-rich gases, *Catal. Today* 158 (2010) 470–474, <https://doi.org/10.1016/j.cattod.2010.07.016>.
- [42] Q. Liu, Z. Liu, L. Liao, X. Dong, Selective CO methanation over amorphous Ni-Ru-B/ZrO<sub>2</sub> catalyst for hydrogen-rich gas purification, *J. Nat. Gas. Chem.* 19 (2010) 497–502, [https://doi.org/10.1016/S1003-9953\(09\)60106-7](https://doi.org/10.1016/S1003-9953(09)60106-7).
- [43] Q. Liu, L. Liao, Z. Liu, X. Dong, Effect of ZrO<sub>2</sub> Crystalline Phase on the Performance of Ni-B/ZrO<sub>2</sub> Catalyst for the CO Selective Methanation, *Chin. J. Chem. Eng.* 19 (2011) 434–438, [https://doi.org/10.1016/S1004-9541\(11\)60003-7](https://doi.org/10.1016/S1004-9541(11)60003-7).
- [44] P.A.U. Aldana, F. Ocampo, K. Kobl, B. Louis, F. Thibault-Starzyk, M. Daturi, P. Bazin, S. Thomas, A.C. Roger, Catalytic CO<sub>2</sub> valorization into CH<sub>4</sub> on Ni-based ceria-zirconia. Reaction mechanism by *operando* IR spectroscopy, *Catal. Today* 215 (2013) 201–207, <https://doi.org/10.1016/j.cattod.2013.02.019>.
- [45] T.A. Le, T.W. Kim, S.H. Lee, E.D. Park, Effects of Na content in Na/Ni/SiO<sub>2</sub> and Na/Ni/CeO<sub>2</sub> catalysts for CO and CO<sub>2</sub> methanation, *Catal. Today* 303 (2018) 159–167, <https://doi.org/10.1016/j.cattod.2017.09.031>.
- [46] A. Petala, P. Panagiotopoulos, Methanation of CO<sub>2</sub> over alkali-promoted Ru/TiO<sub>2</sub> catalysts: I. Effect of alkali additives on catalytic activity and selectivity, *Appl. Catal. B Environ.* 224 (2018) 919–927, <https://doi.org/10.1016/j.apcatb.2017.11.048>.
- [47] X. Wang, Y. Liu, L. Zhu, Y. Li, K. Wang, K. Qiu, N. Tippayawong, P. Aggarangsi, P. Reubroycharoen, S. Wang, Biomass derived N-doped biochar as efficient catalyst supports for CO<sub>2</sub> methanation, *J. COsub2sub Util.* 34 (2019) 733–741, <https://doi.org/10.1016/j.jcou.2019.09.003>.
- [48] E. Kadossow, U. Burghaus, Adsorption Kinetics and Dynamics of CO, NO, and CO<sub>2</sub> on Reduced CaO(100), *J. Phys. Chem. C* 112 (2008) 7390–7400, <https://doi.org/10.1021/jp800755q>.
- [49] D. Li, N. Ichikuni, S. Shimazu, T. Uematsu, Catalytic properties of sprayed Ru/Al<sub>2</sub>O<sub>3</sub> and promoter effects of alkali metals in CO<sub>2</sub> hydrogenation, *Appl. Catal. Gen.* 172 (1998) 351–358, [https://doi.org/10.1016/S0926-860X\(98\)00139-2](https://doi.org/10.1016/S0926-860X(98)00139-2).
- [50] E.H. Cho, Y.-K. Park, K.Y. Park, D. Song, K.Y. Koo, U. Jung, W.R. Yoon, C.H. Ko, Simultaneous impregnation of Ni and an additive via one-step melt-infiltration: Effect of alkaline-earth metal (Ca, Mg, Sr, and Ba) addition on Ni/γ-Al<sub>2</sub>O<sub>3</sub> for CO<sub>2</sub> methanation, *Chem. Eng. J.* 428 (2022) 131393, <https://doi.org/10.1016/j.cej.2021.131393>.
- [51] V. Coman, B. Robotin, P. Ilea, Nickel recovery/removal from industrial wastes: a review, *Resour. Conserv. Recycl.* 73 (2013) 229–238, <https://doi.org/10.1016/j.resconrec.2013.01.019>.
- [52] D. Wang, L. Zhang, K. Kamasamudram, W.S. Epling, In Situ-DRIFTS study of selective catalytic reduction of NO<sub>x</sub> by NH<sub>3</sub> over Cu-exchanged SAPO-34, *ACS Catal.* 3 (2013) 871–881, <https://doi.org/10.1021/cs300843k>.
- [53] H.L. Huynh, J. Zhu, G. Zhang, Y. Shen, W.M. Tucho, Y. Ding, Z. Yu, Promoting effect of Fe on supported Ni catalysts in CO<sub>2</sub> methanation by *in situ* DRIFTS and DFT study, *J. Catal.* 392 (2020) 266–277, <https://doi.org/10.1016/j.jcat.2020.10.018>.
- [54] B.S. Caglayan, İ.İ. Soykal, A.E. Aksoylu, Preferential oxidation of CO over Pt–Sn/AC catalyst: adsorption, performance and DRIFTS studies, *Appl. Catal. B Environ.* 106 (2011) 540–549, <https://doi.org/10.1016/j.apcatb.2011.06.014>.

- [55] T. Burger, P. Donaubauer, O. Hinrichsen, On the kinetics of the co-methanation of CO and CO<sub>2</sub> on a co-precipitated Ni-Al catalyst, *Appl. Catal. B Environ.* 282 (2021) 119408, <https://doi.org/10.1016/j.apcatb.2020.119408>.
- [56] L. Falbo, C.G. Visconti, L. Lietti, J. Szanyi, The effect of CO on CO<sub>2</sub> methanation over Ru/Al<sub>2</sub>O<sub>3</sub> catalysts: a combined steady-state reactivity and transient DRIFT spectroscopy study, *Appl. Catal. B Environ.* 256 (2019) 117791, <https://doi.org/10.1016/j.apcatb.2019.117791>.
- [57] Z. Ma, R. Xiao, H. Zhang, Catalytic steam reforming of bio-oil model compounds for hydrogen-rich gas production using bio-char as catalyst, *Int. J. Hydrog. Energy* 42 (2017) 3579–3585, <https://doi.org/10.1016/j.ijhydene.2016.11.107>.